Boundary-Layer Meteorol. manuscript No.
(will be inserted by the editor)

Laboratory Experiments on Convective Entrainment using a Saline Water Tank

Harmen J.J. Jonker · **Maria A. Jiménez**

Received: date / Accepted: date

Abstract Entrainment fluxes in a shear-free convective boundary layer have been measured with a saline water tank set-up. The experiments were targeted towards measuring the entrainment behaviour for medium to high Richardson numbers and use a two-layer design, i.e. two stacked non-stratified (neutral) layers with different densities. With laser induced fluorescence (LIF), the entrainment flux of a fluorescent dye is measured for bulk Richardson numbers in the range 30-260. It is proposed that a carefully chosen combination of top-down and bottom-up processes improves the accuracy of LIF-based entrainment observations. The observed entrainment fluxes are about an order of magnitude lower than reported for thermal water tanks: the derived buoyancy entrainment ratio, A, is found to be $A \approx 0.02$, which is to be compared with $A \approx 0.25$ for a thermal convection tank (Deardorff et al., J. Fluid Mechanics, 1980, Vol.100, 41–64). An extensive discussion is devoted to the influence of the Reynolds and Prandtl numbers in laboratory experiments on entrainment.

Keywords Convective boundary layer · Entrainment · Laboratory experiments

1 Introduction

For weather, climate and air quality purposes it is of key importance to quantify the deepening rate of a turbulent atmospheric boundary layer into the overlaying free troposphere. The turbulence can originate from a variety of sources, most notably shear and buoyancy. Historically, laboratory experiments targeted to mimic such situations in a downscaled setting, have played an important role in understanding and quantifying the process of deepening mixed layers, in particular the process of entrainment. Two classical examples are the water

Harmen J.J. Jonker
Atmospheric Physics section, department Geoscience and Remote Sensing,
Delft University of Technology, P.O. Box 5048, 2600 GA, Delft, The Netherlands.
E-mail: h.j.j.jonker@tudelft.nl

Maria A. Jiménez
Department of Global Change Research
Institut Mediterrani d'Estudis Avançats, IMEDEA (CSIC-UIB)
Miquel Marquès 21, 07190 Esporles (Illes Balears) Spain
E-mail: majimenez@imedea.uib-csic.es

tank experiments of Kato and Phillips (1969) (deepening by shear), and Willis and Deardorff (1974), Deardorff et al. (1980) (deepening by surface buoyancy).

The advantage of studying entrainment characteristics in the laboratory, rather than outdoors, is that 1) one has control over the initial and boundary conditions, the homogeneity of the surface and the external forcings; 2) the experiments (if conducted well) are reproducible; 3) one can perform parameter studies keeping everything else constant. These aspects, after all, form the cornerstone of scientific research and are not easily realized in atmospheric measurement studies. The major downside of laboratory experiments is their limited scale, or more precise, the fact that the attainable Reynolds and Péclet numbers are orders of magnitude lower than in the geophysical case (the Péclet number is the ratio between the convective contribution and the diffusive contribution to the flux). We come back to this important aspect in Sect. 2 and in the Discussion (Sect. 5). This issue notwithstanding, in particular the thermal convection tank results on penetrative entrainment by Deardorff et al. (1980) have had a big impact in boundary-layer meteorology. As the non-dimensional entrainment rate was found to follow an inverse Richardson law, viz. ARi^{-1} with $A \approx 0.25$, the result appeared to comply with the early views on convective entrainment (Ball 1960; Tennekes 1973) and with atmospheric observations (e.g. Stull 1976, and references therein). This explains why laboratory experiments have formed an important benchmark case for large-eddy simulation (LES) studies (e.g. Nieuwstadt et al. 1993; Sullivan et al. 1998; Fedorovich et al. 2004).

Still there are a few unresolved issues on convective entrainment, in particular the behaviour for large Richardson numbers. Experiments by Turner (1968) showed that, apart from a Ri^{-1} law, also a $Ri^{-3/2}$ law can be observed, which would be even more likely for high Péclet numbers such as in the atmosphere. In this context it is interesting that Deardorff et al. (1980) presented their results in a subtle way: "It [the Ri^{-1} law] appears to represent our data slightly better than the $Ri^{-\frac{3}{2}}$ law". On the other hand, experiments on convective entrainment by Kantha (1980) in a different set-up revealed a 'regime change' at a Richardson number of order 10^2.

Our study is therefore aimed at exploring the entrainment characteristics for relatively high Richardson numbers. To this end we use a saline water tank and conduct experiments in a so-called two-layer arrangement – two stacked non-stratified layers with different densities (Kantha et al. 1977; Kantha 1980). Such an arrangement enables one to create a well-defined buoyancy jump (Richardson number), and to choose settings such that the Richardson number remains constant during an experiment. There are several advantages of a saline water tank over a thermal tank (Hibberd and Sawford 1994a,b): there is, for example, no temperature leakage at the boundaries due to conduction or radiation, and the diffusivity of salt is more than two orders smaller than the diffusivity of heat, which enables one to retain stationary density jumps (see also Sect. 2). A drawback is that the surface buoyancy flux is realized through applying a surface mass flux; as a result, the mixed layer deepens not only due to entrainment but also due to the added mass. On the other hand the advantage of a surface mass flux is that one can readily conduct 'bottom-up' diffusion experiments (Wyngaard and Brost 1984) by adding a dye to the surface inflow – a feature that will be exploited herein together with 'top-down' diffusion.

2 Governing equations

In order to be able to readily compare convection in the saline tank with its geophysical counterpart, as well as with convection in a thermal tank, it is most convenient to formulate

the framework in terms of the buoyancy $b = -g(\rho - \rho_0)/\rho_0$, where ρ denotes the density, ρ_0 is a reference density and g is the acceleration due to gravity. Within the Boussinesq approximation and in the absence of the Coriolis force, the governing equations can be written as

$$\frac{\partial u_i}{\partial t} = -u_j \frac{\partial u_i}{\partial x_j} - \frac{1}{\rho_0}\frac{\partial p}{\partial x_i} + \nu \frac{\partial^2 u_i}{\partial x_j^2} + b\delta_{i3}, \tag{1}$$

$$\frac{\partial u_i}{\partial x_i} = 0, \tag{2}$$

$$\frac{\partial b}{\partial t} = -u_j \frac{\partial b}{\partial x_j} + D\frac{\partial^2 b}{\partial x_j^2}, \tag{3}$$

where u_i $\{i = 1,2,3\}$ denotes the velocity in the x,y,z directions, respectively, with the z-direction pointing upwards, p denotes the pressure, δ is the Kronecker symbol, ν is the kinematic viscosity of the carrier fluid (water/air) in $\mathrm{m}^2\ \mathrm{s}^{-1}$ and D is the molecular diffusivity of the quantity related to buoyancy (i.e. temperature/salinity) in $\mathrm{m}^2\ \mathrm{s}^{-1}$. In the case of convection in the atmospheric boundary layer, b is usually expressed in terms of the virtual potential temperature θ_v through $b = g(\theta_\mathrm{v} - \theta_{\mathrm{v}0})/\theta_{\mathrm{v}0}$ (e.g. Stull 1988). In a thermal convection tank one has $b = g\alpha(T - T_0)$, with T the temperature and α the thermal expansion coefficient of water. In a saline convection tank, on the other hand, density differences arise from the salinity fraction S, i.e. $\rho(S) = \rho_0(1+S)$, with ρ_0 is the density of pure water. The buoyancy is thus related to salinity via

$$b = -gS. \tag{4}$$

In the shear-free convective boundary layer, turbulence is driven by a surface buoyancy flux B. The other relevant aspect defining the case is the initial condition. Instead of the commonly applied linear stratification (constant density gradient), we consider here a so-called *two-layer set-up* (Kantha 1980; Deardorff et al. 1980), i.e. two stacked neutrally stratified layers separated by an initial buoyancy jump Δb at initial height $h(0) = h_0$, see Fig. 1. Due to entrainment the mixed-layer height h will increase

$$w_\mathrm{e} = \frac{\mathrm{d}h}{\mathrm{d}t},$$

where w_e is the entrainment rate. The key question is how w_e can be expressed in terms of the strength of the buoyancy jump (inversion), and the surface buoyancy flux. Equations 1-3 show that the full problem is characterized by 1) the boundary condition B; 2) the initial conditions h_0, Δb; and 3) the fluid properties ν, D. In addition the tank geometry (height-width) may play a role.

Combining these parameters one can define the convective velocity scale (Deardorff 1970)

$$w_* = (Bh)^{1/3} \tag{5}$$

and the large eddy turnover time $t_* = h/w_*$. Rescaling the equations using w_* for velocity, t_* for time, h for length, $\rho_0 w_*^2$ for pressure, and $b_* = B/w_*$ for buoyancy, one obtains

$$\frac{\partial u_i}{\partial t} = -u_j \frac{\partial u_i}{\partial x_j} - \frac{\partial p}{\partial x_i} + \frac{1}{Re}\frac{\partial^2 u_i}{\partial x_j^2} + \delta_{i3} b, \tag{6}$$

$$\frac{\partial b}{\partial t} = -u_j \frac{\partial b}{\partial x_j} + \frac{1}{Pe}\frac{\partial^2 b}{\partial x_j^2}. \tag{7}$$

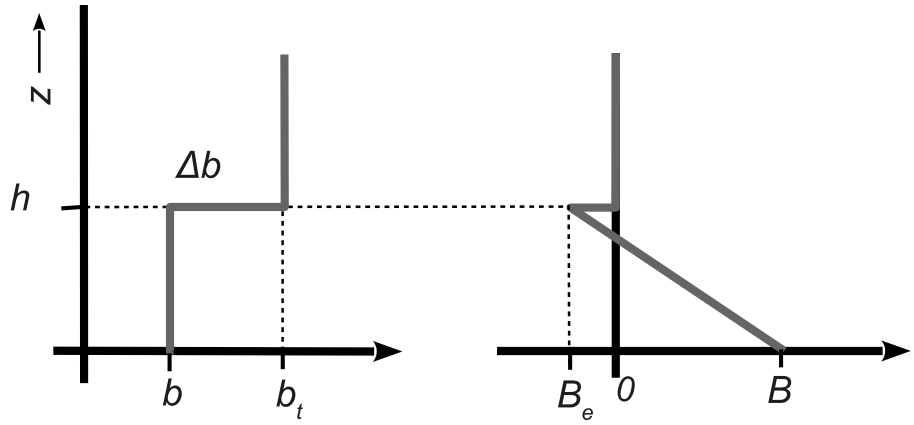

Fig. 1 Zero-order representation of the profiles of buoyancy and the buoyancy flux.

The initial condition, characterized by the buoyancy jump Δb, gives, after rescaling by b_*, the bulk Richardson number $Ri = \Delta b/b_* = \Delta b h/w_*^2$. If one includes the tank geometry, one can conclude that in essence the problem is characterized by four dimensionless numbers, viz. the Reynolds number, the Péclet number, the Richardson number, and the tank aspect ratio

$$Re = \frac{w_* h}{\nu}, \qquad Pe = \frac{w_* h}{D}, \qquad Ri = \frac{\Delta b h}{w_*^2}, \qquad \Gamma = \frac{h}{L}, \tag{8}$$

where L is the lateral size. The non-dimensional entrainment rate $E = w_\mathrm{e}/w_*$ is some function of these dimensionless numbers

$$\frac{w_\mathrm{e}}{w_*} = E(Re, Pe, Ri, \Gamma). \tag{9}$$

Instead of the $\{Re, Pe\}$ combination, one could also use $\{Re, Pr\}$ to define the situation, where $Pr = \nu/D$ is the Prandtl number. Actually, in the case of salinity, it would be more appropriate to refer to ν/D as the Schmidt number, but following e.g. Wolanski and Brush (1975) or Sayler and Breidenthal (1998) hereafter we refer to ν/D as the Prandtl number both for thermal and saline situations.

In laboratory experiments aimed to mimic geophysical phenomena it is usually presumed that the Reynolds number and the Péclet number are *large enough* not to have an important effect on the results (e.g. Townsend 1980; Wyngaard 2010). Molecular properties of the fluid and geometric details of the set-up then play a minor role. In Sect. 5 we come back to the important issue of Reynolds-number independence, because it is not easy to know *a priori* how large the Reynolds number should be to reach this regime. If the regime is reached, the non-dimensional entrainment rate is only dependent on the Richardson number, generally assumed via a power-law relation

$$E(Ri) = aRi^{-b} \tag{10}$$

with a and b constants. As mentioned in the Introduction, the accepted values for atmospheric convection are $a = 0.2 \ldots 0.25$ and $b = 1$. The -1 Richardson-number law is consistent with the common assumption in mixed-layer models (Tennekes 1973) that the entrainment buoyancy flux B_e is a fixed fraction A of the surface buoyancy flux B (Ball 1960).

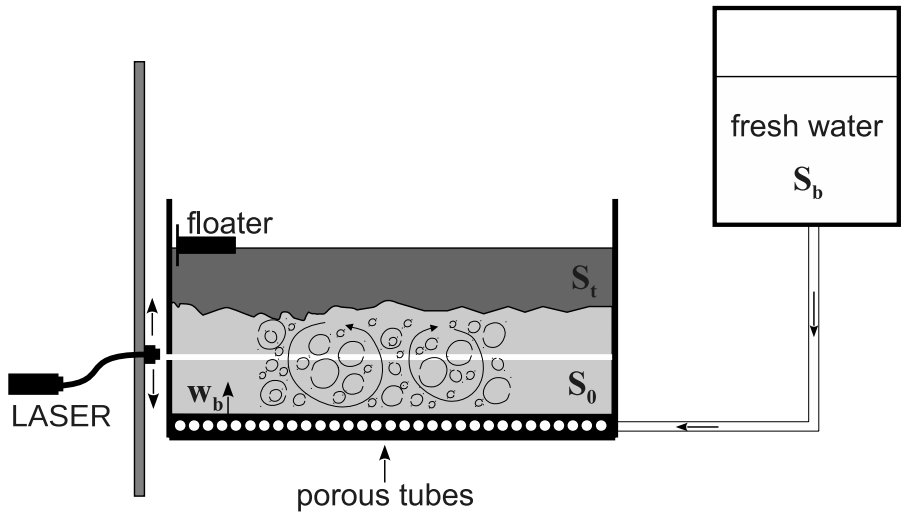

Fig. 2 Sketch of the saline convection tank set-up.

Indeed, invoking a zero-order model (Lilly 1968) for the entrainment flux $B_e = -w_e \Delta b$, using Eq. 10 with the Richardson number defined by Eq. 8, and Eq. 5, gives $A = -B_e/B = a$; see also the sketch in Fig. 1.

In this study we focus on determining A rather than w_e because we are particularly interested in the behaviour at high Richardson numbers. The entrainment rate w_e might become very small for high Ri but, for a Ri^{-1} law, the value of A should be independent of the Richardson number. We emphasize here that, if the entrainment rates in the saline convection tank set-up display an entrainment law with an exponent b different from 1, then the measured values of A will show a Richardson dependence

$$A(Ri) = -B_e/B = E(Ri)\, Ri = aRi^{1-b}. \tag{11}$$

For example, a $Ri^{-3/2}$ law would lead to A vanishing according to $\sim 1/\sqrt{Ri}$. In addition, if the present set-up introduces a Reynolds/Péclet number dependence in the entrainment rate Eq. 9, then this will also show up in the flux ratio, i.e. $A = A(Re, Pe, Ri, \Gamma)$.

3 Experimental set-up and measurement methodology

3.1 Description of the saline tank set-up

The saline convection tank set-up that we used is been sketched in Fig. 2. It consists of a 1m×1m glass container with height 0.5m, a scanning rail, a 2.5W Argon laser connected via an optical fibre to the scanning rail, a digital 10-bit camera located in front of the tank, an elevated water reservoir, and at the bottom of the convection tank a tray consisting of 49 parallel porous tubes (Gardena, external diameter 17 mm). The porous tubes were covered with a carefully levelled bed ($\approx$ 10 mm) of small aquarium quartz pebbles (small reddish stones a few mm in size) to even the surface. Another important experimental issue concerns the spatial homogeneity of the surface fluxes. Tests of the homogeneity of the surface fluxes are described later in this section.

Quantity	Symbol	Typical value	Unit
mixed-layer height (initial)	h_0	0.1	m
bottom inflow	w_b	$2 \cdot 10^{-5}$	m s^{-1}
salinity inflow	S_b	0.0	%
salinity mixed layer (initial)	S_0	0.5	%
salinity top layer	S_t	0.0 — 0.4	%
dye concentration inflow	C_b	0.0	μg l^{-1}
dye concentration mixed layer (initial)	C_0	10	μg l^{-1}
dye concentration top layer	C_t	50 — 200	μg l^{-1}
convective velocity	w_*	$5 \cdot 10^{-3}$	m s^{-1}
eddy turnover time	t_*	20	s
inversion strength (initial)	Ri	50 — 250	-
viscosity	ν	$1 \cdot 10^{-6}$	m^2 s^{-1}
saline diffusivity	D	$1 \cdot 10^{-9}$	m^2 s^{-1}

Table 1 Typical values of parameters used in the set-up.

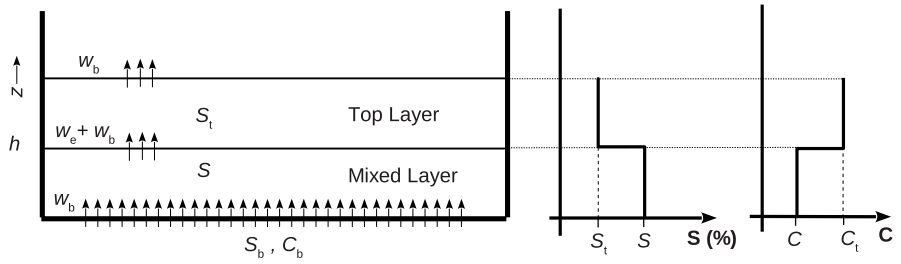

Fig. 3 Schematic view of the two layers separated by a buoyancy jump (left) and corresponding salinity and dye concentration profiles (right). The top water level increases by the inflow rate w_b whereas the mixed layer also grows by entrainment, i.e. at a rate $w_\mathrm{e} + w_\mathrm{b}$.

All entrainment experiments have been conducted within the context of a so-called two-layer set-up (e.g. Kantha et al. 1977; Kantha 1980) such as schematically depicted in Fig. 3. This initial state was created by first filling the tank through the porous tubes with well-mixed water with salinity S_0 up to a height $h_0 \approx 0.1$m. Next a layer with lower salinity S_t was added on top of the mixed layer resulting in a buoyancy jump of $\Delta b = g[S_0 - S_\mathrm{t}]$. Placing this layer on top was done by a careful (slow) filling procedure that consisted of dripping water on top of four floating devices (not depicted in the sketch) that were submerged just below the water surface. Due to the design of these floaters, only a flow in a lateral direction occurs. In this way very sharp buoyancy jumps could be created, which by virtue of the small diffusivity of salinity ($D \approx 10^{-9}$m^2 s^{-1}) remained sharp until the experiment was started. For example, the time for the diffusion region to become $\approx 5\%$ of the initial mixed-layer height, $\delta = 0.05 h_0$, can be estimated by $\delta^2/D \approx 7$hr, i.e. much longer than the typical duration of an experiment (15min). This highlights one of the advantages of the saline set-up over a thermal tank set-up for which the mentioned time scale amounts to only 3min.

After the initial two-layer profile had been created, convection was initiated by supplying water with low salinity S_b from the elevated large reservoir to the porous tubes; the pressure difference due to the elevation is large enough to overcome the hydrodynamic resistance of the porous tubes and gives rise to a homogenous inflow velocity w_b of about 2×10^{-5}m s^{-1}. As will be detailed later, this inflow velocity is more than two orders of magnitude smaller than the convective velocity w_* and therefore has a negligible effect on

the flow in terms of momentum. But the inflow of low density fluid has a strong effect in terms of buoyancy, the resulting surface buoyancy flux being

$$B = g w_\mathrm{b}[S(t) - S_\mathrm{b}] \tag{12}$$

where $S(t)$ denotes the salinity in the mixed layer. Initially $S(t=0) = S_0$, but during the course of the experiment S is diluted due to both the surface and the entrainment salinity flux, which entails that the surface buoyancy flux B decreases during the experiment. This effect will be accounted for in the analysis of the results. It is also important to note that the mixed-layer height $h(t)$ increases not only due to entrainment w_e but also due to the surface mass flux w_b,

$$\frac{\mathrm{d}}{\mathrm{d}t}h = w_\mathrm{e} + w_\mathrm{b}. \tag{13}$$

So it is essential to very accurately measure w_b in the experiments because it directly controls both the mixed-layer height and the surface buoyancy flux. We return to this particular issue in the next section.

Table 1 gives an idea of the typical values we used in the experiments. Using Eq. 12 and Eq. 5 one finds a surface buoyancy flux of $B \approx 10^{-6}$ m^2 s^{-3} and a convective velocity scale of $w_* \approx 5 \times 10^{-3}$ m s^{-1}, respectively, which indicates that the inflow velocity w_b is indeed much smaller than the convective velocity: $w_*/w_\mathrm{b} \approx 250$. The Reynolds number and Péclet number based on w_* (see Eq. 8) are $Re = 500$ and $Pe = 5 \times 10^5$, respectively. The Reynolds number is thus of comparable order as in the thermal convection tank of Deardorff et al. (1980); the Péclet number is however two orders of magnitude larger in the saline set-up due to the much lower diffusivity of salt compared to heat. We address these issues in more detail in the Discussion. At this stage we merely point out that the Reynolds number does not change much during an experiment. Indeed, whereas the increasing mixed-layer depth tends to increase the Reynolds number during the experiments, this effect is largely offset by the decreasing surface buoyancy flux resulting from the gradually decreasing mixed-layer salinity concentration. The net effect is only a slight increase of the Reynolds number during the course of the experiments.

The inversion strength is controlled by the salinity S_t in the upper layer for which we take values ranging between zero and 0.4%. The corresponding Richardson numbers follow from Eq. 8 and can be written as

$$Ri = \frac{\Delta b}{b_*} = \frac{w_*}{w_\mathrm{b}} \, \frac{S - S_\mathrm{t}}{S - S_\mathrm{b}}. \tag{14}$$

Since S decreases during an experiment, so the Richardson number changes. The interesting exception is when $S_\mathrm{t} = S_\mathrm{b}$ for which the Richardson number is nearly constant (because w_* is nearly constant).

3.2 Measuring entrainment with LIF

In order to find the entrainment rate w_e at given Richardson numbers, it would seem natural from Eq. 13 to try and directly measure $\mathrm{d}h/\mathrm{d}t$ and subsequently subtract the measured value of w_b. But such a method fails for moderate to strong inversions because w_e is itself very small and is to be diagnosed from the difference between two relatively large terms, inevitably leading to inaccuracies. For this reason we focus herein on measuring entrainment fluxes rather than entrainment velocities. In the simplest form one can think of adding dye

only to the top layer and diagnosing entrainment from the increasing dye concentration in the mixed layer. An example is given in Fig. 4. These images were not used in the analysis of the results for reasons that will be detailed in the next section, but they nicely show a number of features. One can, for example, clearly make out the cusp-shaped structures of top-layer dye being entrained into the mixed layer; one also sees (in darker shades) the buoyant plumes that impinge on the inversion. Furthermore one can notice the gradual deepening of the mixed layer and that the mixed layer is getting 'greener' due to the entrainment of the dye from the overlaying layer. Such a setting was termed 'top-down diffusion' by Wyngaard and Brost (1984); see also van Dop et al. (2005); Jonker et al. (1999). The advantage of such a setting is that when the entrainment velocity w_e is very low, one can always 'boost' the entrainment flux of the dye, $-w_e(C_t - C)$, by using larger dye concentrations C_t in the top layer. In this way one can adjust the entrainment flux of the dye such that it can be measured with desired accuracy. We use planar laser induced fluorescence (Ferrier et al. 1993; Snyder et al. 2002; van Dop et al. 2005) for measuring the dye concentration in the mixed layer, i.e. by using a fluorescent dye (disodium fluorescein $C_{20}H_{10}O_5Na_2$) that is illuminated by a laser sheet.

We explored a variety of techniques to create a planar laser sheet, such as cylindrical lenses, rotating polygon mirrors, parabolic mirrors, in an effort to create a homogeneous light distribution over the vertical extent of the tank (0.5 m). The best performance in this respect was obtained by directing the laser beam through an optic fibre, the end of which was mounted on a scanning rail that moved up and down in a programmable fashion. The produced narrow vertical laser sheet excited the fluorescent dye in the tank and the resulting fluorescence image was captured by the digital camera located perpendicular to the sheet at about 2 m distance. An optical filter in front of the camera was used to select the wavelengths corresponding to fluorescence and filter out the wavelengths emitted by the Argon laser, which might reach the camera through scattering.

The camera was triggered by the position of the fibre on the transport rail, which enabled us to obtain two types of images: (i) an image of the mixed layer only (type I), and (ii) an image depicting the top layer and the mixed layer together (type II). The advantage of making two separate images is that the measurement of the mixed-layer concentrations in type I images is not disturbed by the high concentrations in the upper layer with high fluorescent intensities, because the camera shutter has already been closed by the time the beam illuminates the top layer. This aspect was found to be very important: in some experiments the top-layer dye concentrations were huge (as compared to the mixed-layer concentrations), so when illuminated by the laser, fluorescent light emitted from the top layer can scatter in the mixed layer; on the camera images it then appears as if the source is in the mixed layer, which leads to an overestimation of the mixed-layer dye concentration. So, by closing the camera shutter before the laser reached the top layer, this cross-talk problem was evaded in image type I.

Image type II, on the other hand, provided useful qualitative information on the structure of the inversion region and the interplay with the convective dynamics. Apart from these qualitative insights, image type II provided important quantitative information on the inflow velocity w_b because it allowed one to track the evolution of the height of the total water column in time. To this end a floating device was placed on top of the water level (see Fig. 2), which is basically a simple piece of foam attached to a small vertical plate that blocks the laser beam when it passes the floater, thus producing a clear demarcation of the water level in the camera image. When the water level rises due to the inflow w_b, the floater will rise at the same speed. From the series of images obtained during the experiment the location of

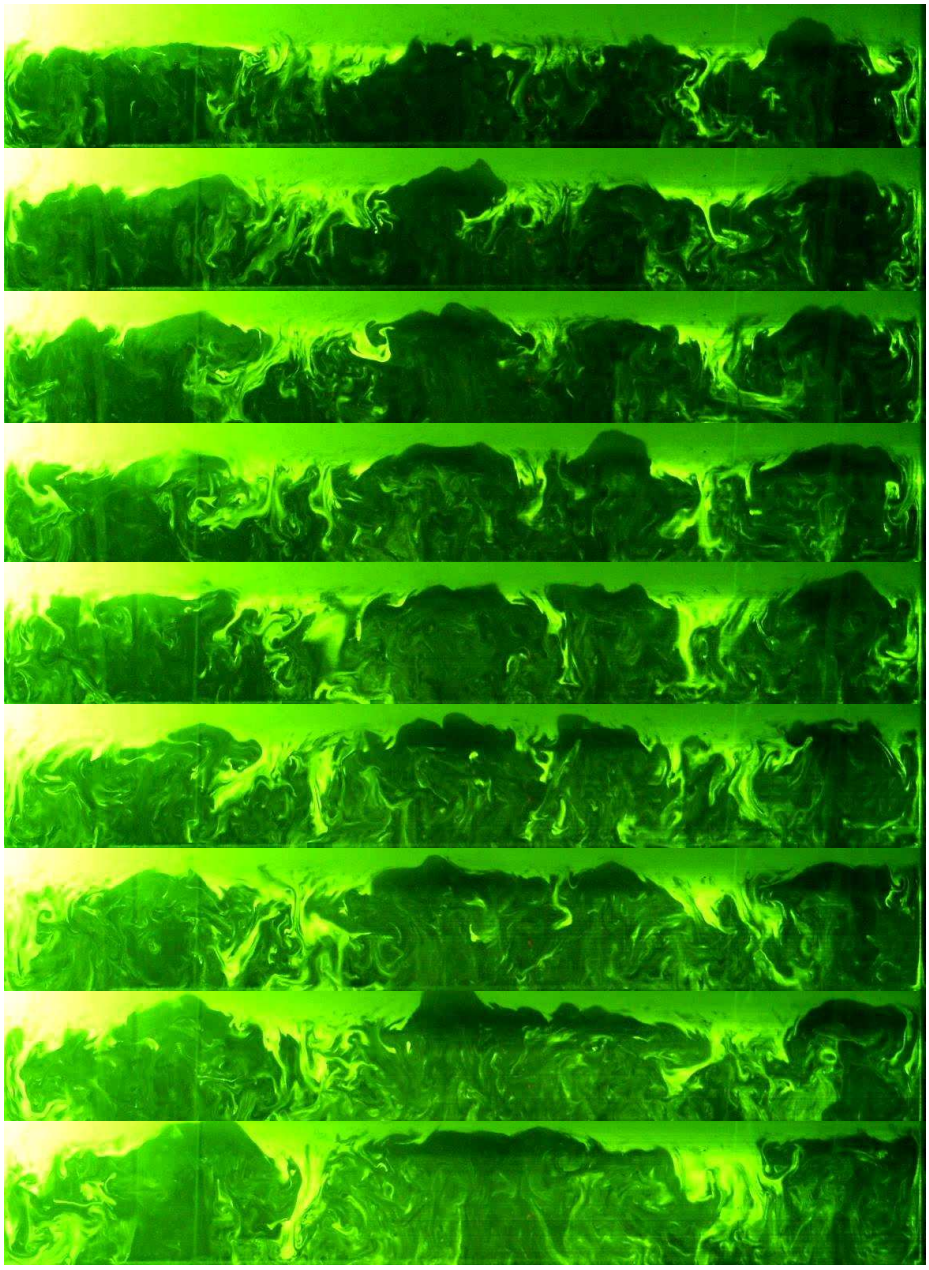

Fig. 4 Example of PLIF images of a top-down scalar at different instances ($t = 14t_*$ to $t = 18t_*$). As explained in the main text, because of the zero initial mixed-layer concentration ($C_0 = 0$), these images are well suited for a qualitative (i.e. visual) analysis but not for a quantitative analysis of entrainment.

the laser-blocking floater is easily extracted, which yielded very accurate measurements of w_b.

To determine the actual dye concentrations from the digital camera images, a few corrections are required, such as deformation of the image and 'pixel vignetting' (Ferrier et al. 1993; Snyder et al. 2002). By photographing a grid consisting of 50 mm squares, located in the tank at the position where the laser sheet normally would be, we concluded that the deformation of the image was very minor and needed no correction. Vignetting (reduction of the brightness in the image periphery compared to the image centre), however, was found to be non-negligible and was subsequently corrected for. The resulting camera intensities $I(x,z)$ are related to the local dye concentration $c(x,z)$ by the Lambert-Beer equation that accounts for the attenuation of the laser beam intensity along its path

$$I(x,z) = \beta Q_0 c(x,z) \exp\left\{-\int_0^x \varepsilon\, c(\xi,z)\mathrm{d}\xi - \eta x\right\}. \tag{15}$$

Here $c(x,z)$ is the fluorescein concentration at position (x,z), ε is the extinction coefficient of fluorescein, η is the extinction coefficient of (non-purified) water, Q_0 is the laser intensity at entrance and β is a proportionality constant that, apart from camera related parameters, includes the fluorescence efficiency of fluorescein (Ferrier et al. 1993). Unfortunately it is a non-trivial matter to solve the inversion problem expressed by Eq. 15, which is required for determining the concentration values $c(x,z)$ from the measured pixel intensities $I(x,z)$. But this issue is not critical because we design the experiment in such a way that there is always a mean dye concentration C in the mixed layer that is much larger than the fluctuations $|c'(x,z)| \ll C$. Equation 15 then simplifies to

$$I(x,z) = \beta Q_0 C \exp\{-(\varepsilon C + \eta)x\}. \tag{16}$$

Fitting a straight line to the logarithm of $I(x,z)$ provides information on C, both through the slope and the abscissa resulting from the fit procedure. The values for the extinction parameters ε and η were determined in a calibration process entailed filling the tank consecutively with 30 known concentrations of fluorescein and recording the corresponding intensities.

Because the laser intensity may vary from experiment to experiment, it was found useful to take several images before initiating the convection. Because we always start with a precisely known dye concentration in the mixed layer we can diagnose in each experiment the proportionality factor βQ_0 in Eq. 16. In principle this information is not needed because the slope of the abovementioned linear fit only requires the value of ε to give C. However we still calculate C in both ways (from the slope and the abscissa) because it provides a consistency check.

During the experiments images (type I and II) were taken every 6s, while all experiments lasted longer than 1000s, i.e. at least $50t_*$. Another important experimental issue concerns the spatial homogeneity of the surface fluxes. As mentioned, the porous tubes are covered with small pebbles, but the finite size of the porous tubes (17 mm diameter) as well as their orientation in one direction might in principle create a spatial pattern. To test whether the surface fluxes were sufficiently homogeneous, we did a number of experiments in which the dye was added to the reservoir tank rather than to the top layer – a so-called 'bottom-up diffusion' set-up. In these experiments the scanning rail was directed in the horizontal, creating horizontal laser sheets while the camera was located above the tank. The observed spatial distributions did not reveal structures with a preferred orientation in one direction or the other. From looking at the images, for example, uninformed observers were unable to determine the orientation of the tubes.

3.3 A mixed-layer model for the saline tank set-up

In order to better understand the results of the saline tank set-up, it proves very useful to consider a simplified model of the saline convection along the lines of the well-known mixed-layer model (Tennekes 1973; Vilà-Guerau de Arellano et al. 2004; van Driel and Jonker 2011) for the atmospheric convective boundary layer. This model needs to be slightly revised for the saline tank due to the mass-flow at the surface that influences the mixed-layer height (Eq. 13) and due to the fact that the surface buoyancy flux (Eq. 12) is not constant. But in all other respects we proceed along the same lines as in the standard mixed-layer model. We also derive prognostic equations for a passive scalar (van Dop et al. 2005), which enables us to compare the model results for the concentrations to the dye concentrations observed in the tank experiments.

Within the mixed-layer assumptions the concentration of salinity in the mixed layer evolves according to the surface flux $\phi_b(t) = -w_\mathrm{b}[S(t) - S_\mathrm{b}]$ and an entrainment flux $\phi_e(t) = -w_\mathrm{e}[S_\mathrm{t} - S(t)]$

$$\frac{d}{dt}S = \frac{\phi_b - \phi_e}{h} = \frac{-w_\mathrm{b}[S(t) - S_\mathrm{b}] + w_\mathrm{e}[S_\mathrm{t} - S(t)]}{h(t)}, \tag{17}$$

while a similar equation holds for the passive scalar concentration

$$\frac{\mathrm{d}}{\mathrm{d}t}C = \frac{-w_\mathrm{b}[C(t) - C_\mathrm{b}] + w_\mathrm{e}[C_\mathrm{t} - C(t)]}{h(t)}, \tag{18}$$

with the mixed-layer height developing according to Eq. 13. The model is closed as described in Sect. 2, i.e. by relating the entrainment rate w_e via a zero-order model to the entrainment flux by $w_\mathrm{e} = -B_e/\Delta b$, while on the other hand expressing the entrainment flux as a (not necessarily constant) fraction of the surface buoyancy flux $B_e = -AB$, leading to

$$w_\mathrm{e}(t) = w_\mathrm{b}\, A\, \frac{S(t) - S_\mathrm{b}}{S(t) - S_\mathrm{t}}. \tag{19}$$

Upon providing initial conditions $h(0) = h_0$, $S(0) = S_0$, $C(0) = C_0$ and boundary conditions S_b, S_t, C_b, C_t, w_b, the equations can be numerically integrated once a value for A has been prescribed. It seems as if we have adopted a Ri^{-1} closure, however, as discussed in Sect. 2, A may contain dependencies on Ri, Re and Pe. In our treatment elaborated in the next section we modify A in order to seek the best correspondence with the experiments, i.e. A can be considered as a fit parameter. Should a $Ri^{-3/2}$ law better represent the entrainment results of the saline tank set-up, then this will become apparent through the resulting best fitting values of A, which in this example would then display a dependence $A \sim Ri^{-1/2}$.

The mixed-layer model, Eqs. 17–19, can be used to optimally design the entrainment experiments. Since the most accurate measurements can be made when the dye concentration in the mixed layer remains roughly constant (that is, within calibration range) during an experiment, we aim to create a situation in which entrainment of higher dye concentrations is balanced by dilution from the surface flux. Equation 18 provides the experimental settings such that C remains (reasonably) constant during the experiment. One notes from Eq. 18 that it is not possible to keep C exactly constant, because S changes in time; however, approximating $S \approx S_0$ one can find settings such that C is stationary during the initial period. Elaborating the entrainment closure (Eq. 19), and taking $C = C_0$, $C_\mathrm{b} = 0$, one finds that the top-layer concentration C_t should then be chosen as

$$C_\mathrm{t} = C_0 \left[1 + \frac{S_0 - S_\mathrm{t}}{S_0 - S_\mathrm{b}} \frac{1}{\hat{A}}\right]. \tag{20}$$

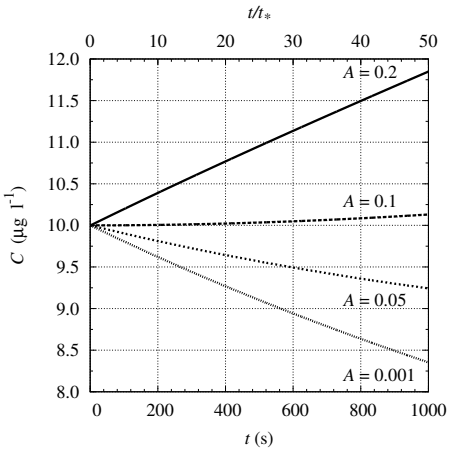

Fig. 5 Evolution of the mixed-layer concentration C as predicted by the mixed-layer model for four different entrainment scenarios. The settings were chosen such that an entrainment ratio of $A = 0.1$ causes the mixed-layer concentration C to remain nearly constant during the experiment. The entrainment flux then balances the surface flux. More entrainment ($A = 0.2$) causes C to increase, whereas less entrainment ($A < 0.1$) entails that C decrease.

Note that C_t in Eq. 20 is based on a *presumed* value of the entrainment ratio, denoted by $\hat{A}$. If during the experiment $C(t)$ is found to increase, one can surmise that the entrainment flux was larger than expected, i.e. that the assumed value of the ratio $\hat{A}$ was too low. On the other hand, if $C(t)$ is found to decrease, the presumed value $\hat{A}$ was too large. In either case one can redo the experiment with initial/boundary conditions based on a refined hypothesis for the entrainment ratio, until a satisfactory stationary state has been reached. To exemplify this idea, we show the results of the mixed-layer equations Eqs. 17–19 for the typical settings given in Table 1. Additionally we took $S_t = 0.2\%$, which corresponds to an initial $Ri = 150$. Using a *presumed* value of $\hat{A} = 0.1$, we find $C_t = 70\mu\text{g l}^{-1}$. Next we integrate the mixed-layer equations for four different 'entrainment scenarios' viz. $A = 0.001, 0.05, 0.1$ and $A = 0.2$. Figure 5 shows what would happen with the mixed-layer concentration $C(t)$ for the four scenarios. When $A = 0.1$, i.e. equal to the presumed value $\hat{A}$, the dye concentration remains reasonably constant – as designed. But if the entrainment is characterized by $A = 0.2$ (twice the 'anticipated' value $\hat{A}$), the concentration increases significantly during the experiment. When A is lower than the anticipated value, concentrations show a marked decrease. In both situations the deviations from the expected equilibrium concentrations are significant enough to be captured by the experimental technique. And, as mentioned, based on the results one can adapt the hypothesis for $\hat{A}$, and conduct a new experiment with modified top concentration C_t.

3.4 Extracting additional information

It is also possible to diagnose additional information from the concentration measurements, such as the mixed-layer salinity and the evolution of the Richardson and Reynolds number. To this end we follow a bulk mixing approach that can be best explained using Fig. 6. Starting with a concentration C_0, which is well mixed over a depth h_0 (step 1 in Fig. 6), at time t the mixed-layer height will have increased due to the mass inflow $h_b = \int_0^t w_b \mathrm{d}t$ and

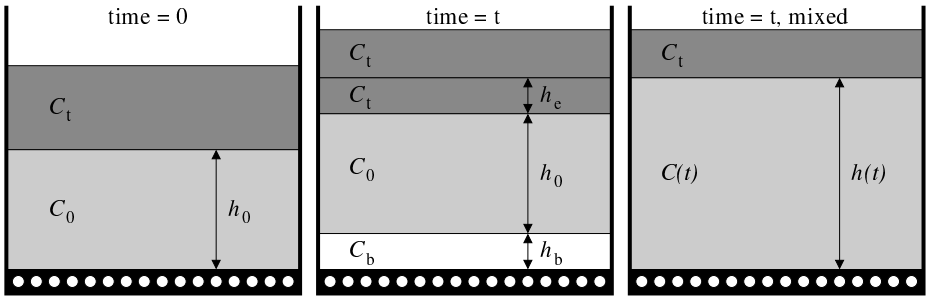

Fig. 6 Evolution of the mixed-layer height $h(t)$ and mixed-layer concentration $C(t)$ as a result of bottom-up (surface inflow) and top-down (entrainment) processes.

due to entrainment $h_e = \int_0^t w_e \mathrm{d}t$, i.e.

$$h(t) = h_0 + h_b(t) + h_e(t). \tag{21}$$

The inflow is associated with a concentration C_b, whereas entrainment infuses concentrations C_t (step 2 in Fig. 6); the turbulent mixing of these contributions results in a new mixed-layer concentration (step 3 in Fig. 6)

$$C(t) = \frac{C_0 h_0 + C_b h_b(t) + C_t h_e(t)}{h_0 + h_b(t) + h_e(t)}. \tag{22}$$

In the experiment C_0, C_t and h_0 are known, and both $C(t)$ and $h_b(t)$ are carefully measured as outlined in Sect. 3.2; it is therefore possible to derive $h_e(t)$ from Eq. 22,

$$h_e(t) = \frac{[C(t) - C_b]h_b(t) + [C(t) - C_0]h_0}{C_t - C(t)}. \tag{23}$$

Once $h_e(t)$ has been determined one can also derive the salt concentration in the mixed layer by an equation equivalent to Eq. 22,

$$S(t) = \frac{S_0 h_0 + S_b h_b(t) + S_t h_e(t)}{h_0 + h_b(t) + h_e(t)}. \tag{24}$$

It is therefore possible to calculate the evolution of the Richardson number (Eq. 14) during the experiment, as well as the evolution of the surface buoyancy flux (Eq. 12), the convective velocity scale w_* (Eq. 5), and the Reynolds number (Eq. 8).

Last but not least we can derive the entrainment ratio from its definition $A = -B_e/B$, in which B_e can be obtained from $\mathrm{d}b/\mathrm{d}t = (B - B_e)/h$. Expressed in terms of salinity this amounts to determining

$$A = -\left[1 + \frac{h(t)}{w_b(S - S_b)} \frac{\mathrm{d}S}{\mathrm{d}t}\right] \tag{25}$$

for which we need Eq. 24, Eq. 21 and Eq. 23, respectively. We tested this method on the time series of $C(t)$ generated by the mixed-layer model (see, for example, Fig. 5) for different entrainment scenarios, and found excellent agreement between the diagnosed value of the entrainment ratio and the value of A that was used to generate the data. When applied to the real measurements, Eq. 25 produces significant scatter in the instantaneous values, which is why we report the average values of an experiment together with error bars to give an indication of the variability.

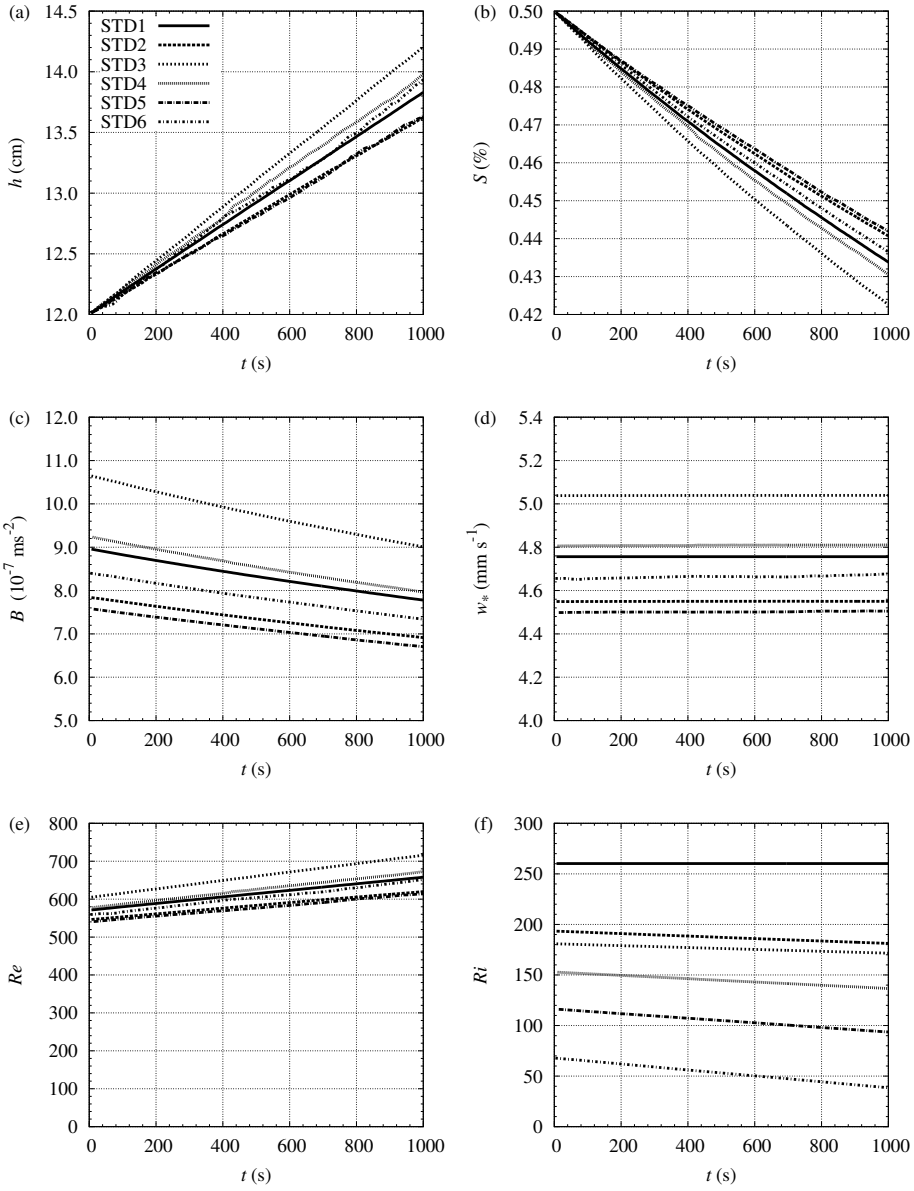

Fig. 7 Evolution of the derived quantities in experiments STD1-6. See Table 2 for the particular settings in each experiment. (a) mixed-layer depth $h(t)$; (b) mixed-layer salinity $S(t)$; (c) surface buoyancy flux $B(t)$; (d) convective velocity scale $w_*(t)$; (e) Reynolds number; (f) Richardson number.

Exp.	S_0 (%)	S_t (%)	S_b (%)	C_t (μg l^{-1})	w_b (m s^{-1})	h_0 (m)	$\langle Ri \rangle$	$\langle Re \rangle$
STD1	0.50	0.00	0.00	210	$1.83{\cdot}10^{-5}$	0.12	260	619
STD2	0.50	0.16	0.00	140	$1.60{\cdot}10^{-5}$	0.12	187	583
STD3	0.50	0.11	0.00	164	$2.17{\cdot}10^{-5}$	0.12	176	660
STD4	0.50	0.20	0.00	70	$1.89{\cdot}10^{-5}$	0.12	145	625
STD5	0.50	0.30	0.00	85	$1.55{\cdot}10^{-5}$	0.12	105	578
STD6	0.50	0.38	0.00	50	$1.71{\cdot}10^{-5}$	0.12	53	605
LRE1	0.50	0.40	0.40	95	$1.89{\cdot}10^{-5}$	0.03	94	71
LRE2	0.50	0.34	0.40	85	$2.00{\cdot}10^{-5}$	0.03	160	73
LRE3	0.50	0.34	0.40	85	$1.96{\cdot}10^{-5}$	0.03	161	72
MRE1	0.11	0.00	0.00	200	$1.91{\cdot}10^{-5}$	0.12	152	379
HRE1	4.00	2.80	0.00	60	$1.89{\cdot}10^{-5}$	0.12	124	1261
HRE2	4.00	3.50	0.00	50	$1.89{\cdot}10^{-5}$	0.12	49	1200

Table 2 An overview of the settings in the various experiments. In all experiments the initial fluorescein concentrations in the mixed layer is $C(0) = C_0 = 10$ μg l^{-1} and in the bottom layer $C_b = 0$. The indicated Richardson and Reynolds numbers are average values; their evolution during the experiments is shown in Fig. 7.

4 Results

Figure 7 shows the evolution of a number of key quantities during experiments STD1–STD6, i.e. the evolution of the mixed-layer depth $h(t)$, the salinity concentration $S(t)$ in the mixed layer, the surface buoyancy flux $B(t)$, the convective velocity scale $w_*(t)$, the Reynolds number and the Richardson number. The figure shows that the mixed-layer salinity decreases, and therefore also the surface buoyancy flux; the convective velocity scale w_* remains constant because the product of h and B is constant. The Reynolds number, $Re = w_* h(t)/\nu$, therefore increases somewhat during an experiment. In experiments STD1–6 we chose to use the same value for the initial mixed-layer salinity, $S_0 = 0.5\%$, in order to set the Reynolds numbers at roughly the same value. The Richardson number was then controlled by the choice of the top-layer salinity S_t. Richardson numbers up to 260 were studied, and several experiments (STD1,LRE1,MRE1) were designed such that the Richardson number does not alter during an experiment; this was done by choosing $S_t = S_b$, see Eq. 14. In the other experiments $S_t \neq S_b$, entailing that the Richardson number changes during the experiment.

In order to measure entrainment fluxes, an appreciable number of experiments was carried out following the principles outlined in Sect. 3.3, that is, the top layer was coloured with dye concentration C_t based on a presumed entrainment ratio $\hat{A}$ as described by Eq. 20. If during the experiment the *real* entrainment ratio A were equal to $\hat{A}$, the mixed-layer concentrations C would be virtually constant because dilution by the surface flux is then just compensated by the entrainment flux. We started out by choosing $\hat{A} = 0.2$, close to the accepted value for atmospheric free convection. But invariably we were confronted with decreasing fluorescein concentrations in the mixed layer, indicating that the actual entrainment flux in the saline tank was significantly lower than anticipated. A new series of experiments based on $\hat{A} = 0.1$ yielded comparable results (see, for example, experiment STD4). Finally we based the top-layer dye concentration in all experiments (except STD4) on $\hat{A} = 0.05$.

Figure 8 shows the measured fluorescein concentrations; as one can observe, in all experiments the mixed-layer concentrations C *decrease*. The inevitable conclusion is therefore that in all experiments the entrainment ratio was *lower* than $A = 0.05$. As an aid to the eye we have also indicated in the figure the predictions by the mixed-layer model (Eqs. 17–19) for

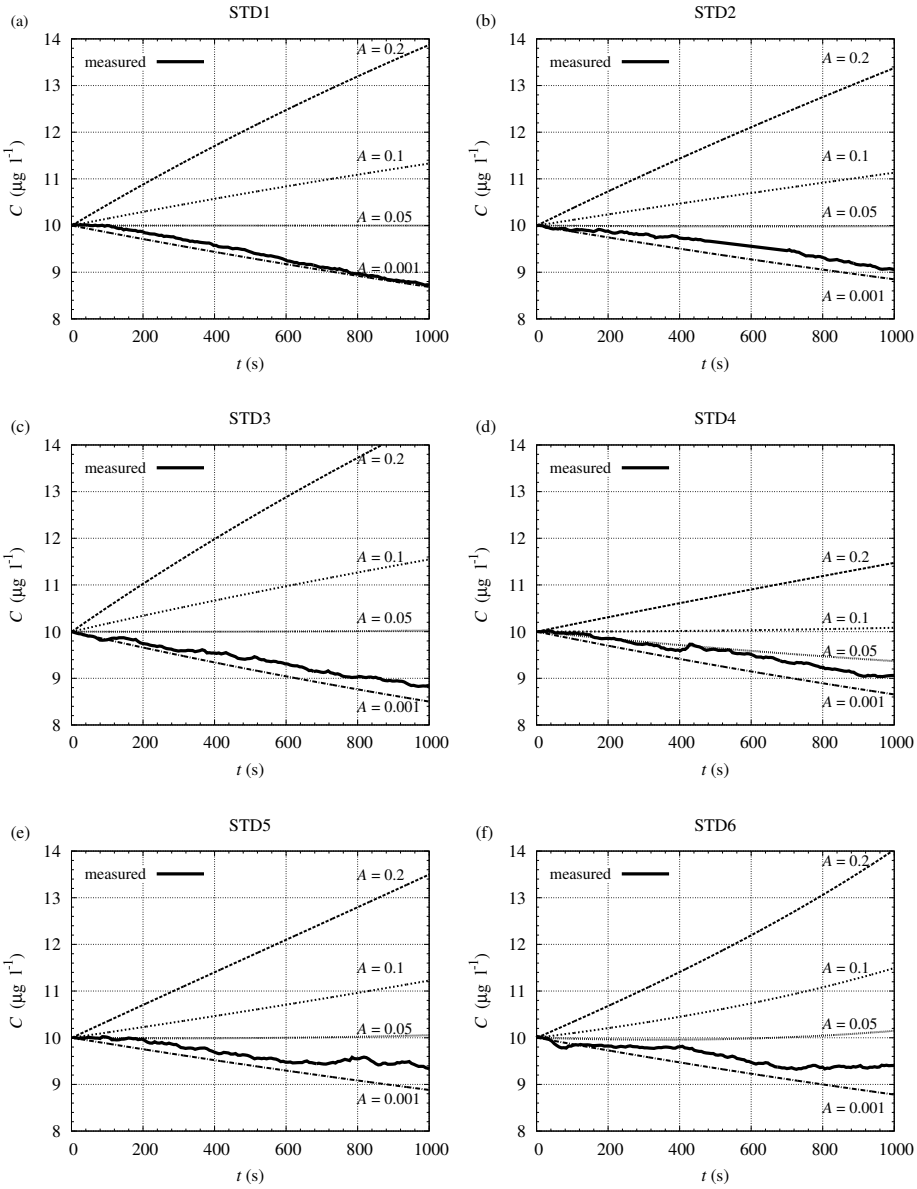

Fig. 8 Evolution of the measured fluorescein concentration in the mixed layer (C) indicated by the solid line. See Table 2 for the particular settings in each experiment. Dotted lines show the evolution as predicted by the mixed-layer model (Eqs. 17–19) for four different entrainment scenarios: $\hat{A} = 0.2$, 0.1, 0.05 and 0.001.

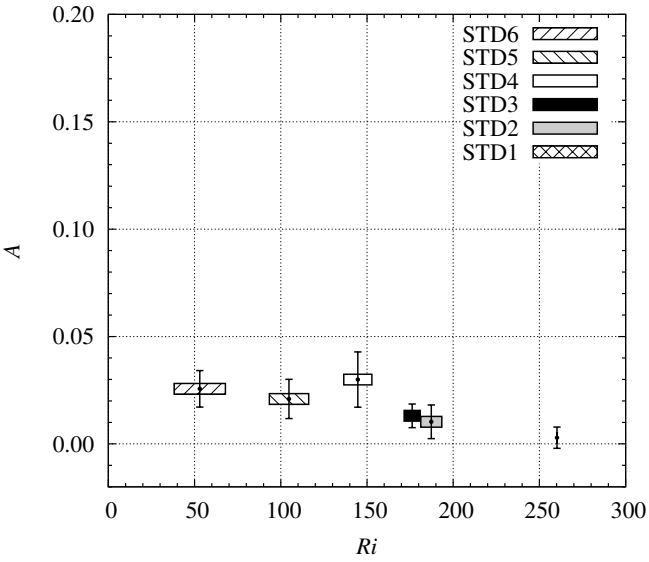

Fig. 9 Entrainment ratio A as a function of the Richardson number. The vertical bars indicate the error in the mean. The horizontal size of the box indicates the range in which the Richardson number varied during the experiment (see Table 2).

four different entrainment scenarios $A = 0.2, 0.1, 0.05$ and 0.001 (virtually a non-entraining situation). From the evolution of $C(t)$ with respect to the cones delineated by the mixed-layer predictions, one can conclude that an entrainment ratio close to $A = 0.02$ would be most appropriate to represent the experimental results. That is more than ten times lower than $A = 0.25$, the entrainment ratio reported for a thermal convection tank set-ups, (Deardorff et al. 1980; Fernando and Little 1990).

From these data we have calculated the average value of the entrainment ratio by means of Eq. 25 and plotted the result as a function of the average Richardson number in Fig. 9. Horizontal bars indicate the Richardson number range, whereas vertical bars indicate the error in the mean as determined from the series of instantaneous values. Clearly there is appreciable scatter, but the mean values display a clear signal and appear to be well in agreement with the early conclusion drawn from Fig. 8 that $A \approx 0.02$. Figure 9 might suggest that the flux ratio even decreases for larger Richardson numbers. Given the appreciable scatter it is unclear whether this points to a $E \sim Ri^{-3/2}$ entrainment law (Turner 1968), or whether the data hint at a 'regime change' (near $Ri \sim 150$) as purported by Kantha (1980). But this issue seems of lesser importance as compared to the result that A has so low a value in the entire Richardson number range – the entrainment fluxes are so small that it seems hardly relevant that they become even lower for larger Richardson numbers.

Because of the large discrepancy between the accepted value of A and the saline convection tank results presented here, a number of additional tests was carried out to check the validity of our measurement method. Since our data are primarily based on concentration measurements, we performed the following tests (the list is not exhaustive):

1) Stability of the fluorescent dye. This was tested by setting-up and conducting an experiment in the normal fashion, but without initiating convection ($w_b = 0$). In the absence of

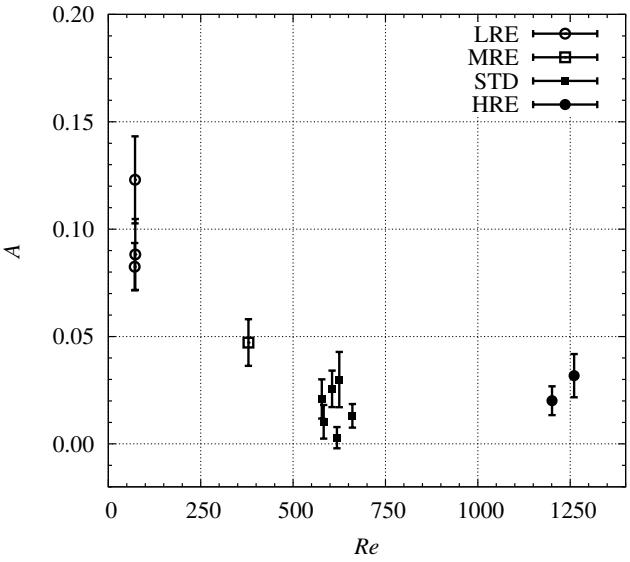

Fig. 10 Entrainment ratio A as a function of the (average) Reynolds number (Richardson numbers vary between experiments, see Table 2). Vertical bars indicate the error in the mean.

surface inflow and dynamics, the mixed-layer concentration must remain constant since, as discussed in Sect. 3.1, molecular diffusion is very small in a saline tank set-up. Whether also the *measured* concentrations remained constant was tested because the fluorescence efficacy of the dye might autonomously decay (due to aging, or overexposure by the laser sheet). However, the concentrations measurements were found to be satisfactorily constant within the duration of an experiment.

2) Study of a non-entraining case. In this test the top layer was not added, but convection was initiated in the usual way resulting in a well-mixed turbulent layer, which grows due to the surface mass inflow but not due to entrainment. The measured mixed-layer concentrations were found to decrease as expected on the basis of the surface dilution (which is known because w_b is measured). Also the reversed situation was tested where $C_\mathrm{b} > C_0$, i.e. a 'bottom-up' case. Concentrations increased according to the expectations.

3) Direct determination of the entrainment velocity. The images captured during the experiments were reanalyzed to determine the evolution of the mixed-layer height h directly by locating the concentration jump in the images (type II). The entrainment rate was subsequently derived from $\mathrm{d}h/\mathrm{d}t - w_\mathrm{b}$. As argued in Sect. 3.2 such a method is prone to inaccuracies, but we employed it nonetheless to look for potential large inconsistencies with the concentration method. However, no such inconsistencies were detected.

These tests further strengthened the conclusion that the entrainment flux in our saline convection tank set-up was about an order of magnitude lower than expected for penetrative convection.

5 Discussion and conclusion

Because the saline convection tank was built so as to serve as a physical model for the atmospheric convective boundary layer, it is important how to interpret the present entrainment results. Not only is there a discrepancy with previous convection tank experiments (Deardorff et al. 1980; Fernando and Little 1990) but also with recent atmospheric observations which put A in the range 0.1—0.4 (Betts and Ball 1994; Angevine et al. 1998) and sometimes even higher (Hägeli et al. 2000). Three items are important in this discussion: 1) the two-layer set-up; 2) the mixed-layer approach to analyze and interpet the data, and 3) the potential influence of molecular properties of the working fluid, i.e. viscosity and diffusivity, or in terms of dimensionless numbers, the influence of the Reynolds and the Péclet number.

5.1 Two-layer set-up

The two-layer set-up, in particular the neutral top layer, differs from a linearly stably stratified upper layer in that a neutral top layer does not sustain buoyancy waves. But it is not directly clear why the absence of waves would *reduce* entrainment; the argument (e.g. Stull 1976; Fedorovich and Mironov 1995) that part of the kinetic energy might be transported through the interface to be transferred to wave energy in the upper layer, works in the opposite direction, i.e. absence of waves in the two-layer set-up leaves more energy for entrainment. Of course also in the two-layer set-up a stable interfacial layer is formed resulting from the system dynamics itself, i.e. the interplay of convection-diffusion, creating some inversion thickness. Indeed, in animations of the camera images travelling waves along the interface were frequently observed, in particular for the higher Richardson numbers. But these waves were not found to break and appeared unable to 'corrupt' the interface and initiate appreciable entrainment.

5.2 Mixed-layer analysis

In the current set-up entrainment information was retrieved by diagnosing the evolution of the mean dye concentration in the mixing layer. To this end a mixed-layer model was invoked that was adapted to the saline tank setting. The results could therefore be affected if the mixed-layer approach is invalid or introduces a significant bias. In fact, the images presented in Fig. 4 might question the validity of the mixed-layer view. We emphasize, however, that these type of images, although visually appealing, were not used in the analysis of entrainment because a variety of optical effects hamper a quantitative interpretation of the image. For reasons detailed in Sect. 3.2, it was better to raise the mean concentration in the mixed layer such that entrainment is balanced by surface dilution. The resulting, uniformly green, images corroborate the validity of the mixed-layer view. In addition it is important to note that, as mentioned in point 3 of the previous section, we also directly measured the mixed-layer depth. The results turned out to be consistent with each other in the sense that both methods show a very slowly deepening boundary layer. This implies that if the mixed-layer approach was inappropriate while in reality the layer was deepening much faster, then this would have shown up in the direct measurements of the layer depth.

5.3 Reynolds number dependence

The next important issue is the influence of (geometrical) details and molecular fluid properties. As mentioned earlier, the general idea is that these details should not matter when the Reynolds number is large enough. Problem is that it is unclear *a priori* what 'large' means for a certain flow configuration. For the present set-up both the geometry and Reynolds number range were deliberately chosen to be comparable to the set-up of Deardorff et al. (1980), which after all is used as a benchmark in a large number of studies. In order to study the influence of the Reynolds number we conducted additional experiments with Reynolds numbers ten times smaller (LRE), two times smaller (MRE), and two times larger (HRE) than the STD experiments. Due to practical limitations it is not easy to change the Reynolds number drastically. For instance, the high Reynolds number cases were realized by increasing the mixed-layer salinity S_0, whereas the low Reynolds number cases were realized by lowering h_0 and reducing the salinity contrast $S_0 - S_\mathrm{b}$; see Table 2. The results for the entrainment ratio A as a function of Re are plotted in Fig. 10 for all experiments regardless of the Richardson number. Interestingly, and perhaps unexpectedly, one observes that in the figure that A *decreases* for increasing Re and then levels off. It is hard to speculate what would happen for much larger Reynolds numbers, but as regards to Fig. 10 we cannot observe a 'worrying' increasing trend in A. Of course the Reynolds numbers are much smaller than is associated with atmospheric convection, $Re \approx 10^8$, based on $h = 10^3$m, $w_* = 1$ m s^{-1}, $\nu \approx 10^{-5}$m^2 s^{-1}. But it is important to realize that if the Reynolds numbers in this study are deemed not large enough, then the same conclusion must drawn for the thermal tank set-up of Deardorff et al. (1980), which takes away an important assumption that $A = 0.25$ for free convection. In addition, if one considers the Péclet number, one has $Pe \approx 10^8$ for the atmospheric situation, $Pe \approx 10^6$ for the saline tank set-up and $Pe \approx 10^4$ for a typical thermal tank set-up. So from the perspective of the Péclet number the saline tank is closer to atmospheric convection than a thermal tank. Turner (1968) suspected that the Péclet number could be too low in a thermal set-up; see also the discussion on thermal convection tanks in Turner (1973). However, Fernando and Little (1990) conducted a comprehensive study on the impact of the Péclet number in a thermal set-up but could not detect any significant influence and confirmed the results of Deardorff et al. (1980).

5.4 Prandtl number dependence

It is very disturbing that different – carefully executed – laboratory studies of the same geophysical phenomenon give such different results. This holds in particular for experiments on entrainment, see the review on laboratory experiments by Fernando (1991). But at least one clear pattern seems to emerge, namely that laboratory experiments with low diffusivity fluids (i.e. with a high Prandtl number) tend to entrain much less. If one looks closely at the buoyancy flux profiles in the saline tank experiments of van Dop et al. (2005) (their figure 7), one notices quite small entrainment fluxes as well. The discrepancy between thermal and saline arrangements was already observed by Turner (1968) for entrainment induced by decaying forced convection (oscillating grid turbulence). Wolanski and Brush (1975) extended Turner's study in a similar set-up but with different solvents (salt, sugar, clay, etc) and found a strong dependence of the Prandtl number (actually Schmidt number) on the entrainment rates.

In this context it is also important to consider the entrainment experiments of Sayler and Breidenthal (1998). Their experimental setting was different to the extent that the case of ra-

diatively driven entrainment was studied mimicking stratocumulus clouds, yet the observed entrainment rates displayed a clear dependence on whether the stratification was applied by heat, $w_e/w_* = 0.25Ri^{-1}$, or by dextrose, $w_e/w_* = 0.08Ri^{-1}$. So the prefactor, i.e. the entrainment flux ratio A, revealed a strong Prandtl number dependence. Interpretation of this result is complicated by the fact that the turbulence in both cases was generated by thermal effects, while the stratification was applied by either heat or by salinity, so the effects of the Prandtl/Schmidt number are convoluted in this setting.

In the same vein we could summarize for free penetrative convection: heat $w_e/w_* \approx 0.25Ri^{-1}$ (Deardorff et al. 1980; Fernando and Little 1990), salt: $w_e/w_* \approx 0.02Ri^{-1}$ (this study and van Dop et al. 2005). But such a state of affairs is entirely unsatisfactorily when it comes to the generalization to atmospheric cases, and, as such, it fails to sufficiently constrain model predictions. An excellent example in this regard is the LES intercomparison study targeted at the so-called 'smoke case' (Bretherton et al. 1999): noting in the experiments of Sayler and Breidenthal (1998) that A increased by a factor 6 when the Prandtl number decreased from 1000 to 7, an *ad hoc* power law dependence $A \sim Pr^{-\gamma}$ was invoked, which was subsequently extrapolated to the atmospheric case of $Pr = 0.7$; this then yielded $A = 0.4$ – a value much closer to the prevailing LES results. If, purely for the sake of the argument, we apply the same procedure for the dry CBL based on $A = 0.25$ for $Pr = 7$ and $A = 0.02$ for $Pr = 10^3$, we would obtain $A = 0.8$ for air. This value is clearly unacceptably high and underlines the problem of ambiguous data from laboratory experiments.

5.5 Outlook

Since the Prandtl number is the ratio between two molecular properties of the fluid, and since Reynolds number similarity requires results to become independent of molecular properties, it seems fair to conclude that laboratory experiments on (convective) entrainment are still very much hampered by the low magnitude of the Reynolds number. There seem to be two viable options to better understanding the reason for the different entrainment results and resolve the impasse. First, one could make use of the newly available supercomputing resources and conduct direct numerical simulations (DNS) of the cases. Clearly, the atmospheric Reynolds number is out of reach for DNS, but present resources allow for significantly larger Reynolds numbers than the original laboratory experiments (e.g. Mellado 2012; Jonker et al. 2013).

Second, one could attempt to reach much larger Reynolds numbers in the laboratory. This can be done by using a different fluid, such as cryogenic helium gas, employed for high Rayleigh number experiments (e.g. Niemela et al. 2000). Or one could try to significantly upscale the water tank set-up. For a saline set-up, such an endeavour is challenging but not inconceivable. Apart from increasing h, the surface buoyancy flux B can be increased by increasing w_b. Limiting the inflow velocity to $w_b = w_*/100$ in order not to disturb the flow, one finds via Eq. 5 and Eq. 12 that $w_* \sim h^{1/2}$ and hence $Re \sim h^{3/2}$. Together with some room for increasing the mixed-layer salinity, it turns out that a swimming pool size set-up allows for a Reynolds number hundred times larger than that achieved in the present study. Such an experiment would be very worthwhile as it will shed light on the Reynolds number influence on convective entrainment of a high Prandtl number fluid. This is an outstanding question, not only from a basic fluid mechanics perspective, but also with respect to the oceanic mixed layer where salinity directly influences buoyancy.

Acknowledgements The authors thank Jos Verdoold, Thijs Heus, Esther Hagen, Jeroen Lebouille, Daniel Abrahams, Erwin de Beus and Rob Rodink for their efforts towards improving the set-up. One of us (MAJ) acknowledges research project CGL2006-12474 from the Spanish Government.

References

Angevine WM, Grimsdell AW, McKeen SA, Warnock JM (1998) Entrainment results from the flatland boundary layer experiments. J Geophys Res 103:13,689–13,701

Vilà-Guerau de Arellano J, Gioli B, Miglietta F, Jonker HJJ, Baltink HK, Hutjes RWA, Holtslag AAM (2004) Entrainment process of carbon dioxide in the atmospheric boundary layer. J Geophys Res 109:D18,110

Ball FK (1960) Control of the inversion height by surface heating. Quart J Roy Meteor Soc 86(370):483–494

Betts AK, Ball JH (1994) Budget analysis of fife 1987 sonde data. J Geophys Res 99:3655–3666

Bretherton CS, MacVean MK, Bechtold P, Chlond A, Cuxart J, Khairoutdinov M, Kosovic B, Lewellen D, Moeng CH, Siebesma AP, Stevens B, Stevens DE, ISykes, Wyant MC (1999) An intercomparison radiatively-driven entrainment and turbulence in a smoke cloud, as simulated by different numerical models. Quart J Roy Meteor Soc 125:391–423

Deardorff JW (1970) Convective velocity and temperature scales for the unstable boundary layer and the Rayleigh convection. J Atmos Sci 23:1211–1213

Deardorff JW, Willis GE, Stockton BH (1980) Laboratory studies of the entrainment zone of a convectively mixed layer. J Fluid Mech 100:41–64

van Dop H, van As D, van Herwijnen A, Hibberd MF, Jonker H (2005) Length scales of scalar diffusion in the convective boundary layer: Laboratory observations. Boundary-Layer Meteorol 116(1):1–35

van Driel R, Jonker HJJ (2011) Convective boundary layers driven by nonstationary surface heat fluxes. J Atmos Sci 68:727–738

Fedorovich E, Mironov D (1995) A model for a shear-free convective boundary layer with parameterized capping inversion structure. J Atmos Sci 52:83–95

Fedorovich E, Conzemius R, Mironov D (2004) Convective entrainment into a shear-free, linearly stratified atmosphere: Bulk models reevaluated through large-eddy simulations. J Atmos Sci 61:281–295

Fernando HJS (1991) Turbulent mixing in stratified fluids. Annu Rev Fluid Mech 23:455–493

Fernando HJS, Little L (1990) Molecular-diffusive effects in penetrative convection. Phys Fluids A 2:1592–1596

Ferrier AJ, Funk DR, Roberts PJW (1993) Application of optical techniques to the study of plumes in stratified fluids. Dyn Atmos Oceans 20:155–183

Hägeli P, Steyn DG, Strawbridge KB (2000) Spatial and temporal variability of mixed-layer depth and entrainment zone thickness. Boundary-Layer Meteorol 97:47–71

Hibberd MF, Sawford BL (1994a) Design criteria for water tank models of dispersion in the planetary convective boundary layer. Boundary-Layer Meteorol 67:97–118

Hibberd MF, Sawford BL (1994b) A saline laboratory model of the planetary convective boundary layer. Boundary-Layer Meteorol 67:229–250

Jonker HJJ, Duynkerke P, Cuijpers JWM (1999) Mesoscale fluctuations in scalars generated by boundary layer convection. J Atmos Sci 56:801–808

Jonker HJJ, van Reeuwijk M, Sullivan PP, Patton EG (2013) On the scaling of shear-driven entrainment: a DNS study. J Fluid Mech 732:150–165

Kantha L (1980) Turbulent entrainment at a buoyancy interface due to convective turbulence. In: Freeland H, Farmer D, Levings C (eds) Fjord Oceanography, Plenum, New York, 205–213

Kantha LH, Phillips OM, Azad RS (1977) On turbulent entrainment at a stable density interface. J Fluid Mech 79:753–768

Kato H, Phillips OM (1969) On the penetration of a turbulent layer into stratified fluid. J Fluid Mech 37(04):643–655

Lilly DK (1968) Models of cloud-topped mixed layers under a strong inversion. Quart J Roy Meteor Soc 94:292–309

Mellado JP (2012) Direct numerical simulation of free convection over a heated plate. J Fluid Mech 712:418–450

Niemela JJ, Skrbek L, Sreenivasan KR, Donnelly RJ (2000) Turbulent convection at very high Rayleigh numbers. Nature 404:837–840

Nieuwstadt F, Mason P, Moeng CH, Schumann U (1993) Large-eddy simulation of the convective boundary layer: A comparison of four computer codes. In: Durst F, Friedrich R, Launder B, Schmidt F, Schumann U, Whitelaw J (eds) Turbulent Shear Flows 8, Springer Berlin Heidelberg, 343–367

642 Sayler BJ, Breidenthal RE (1998) Laboratory simulations of radiatively induced entrainment in stratiform
643 clouds. J Geophys Res 103:8827–8838
644 Snyder WH, Lawson, JR RE, Shipman MS, Lu J (2002) Fluid modelling of atmospheric dispersion in the
645 convective boundary layer. Boundary-Layer Meteorol 102:335–366
646 Stull RB (1976) The energetics of entrainment across a density interface. J Atmos Sci 33:1260–1267
647 Stull RB (1988) An introduction to boundary layer meteorology. Kluwer Acad Publishers, Dordrecht, 666
648 pp.
649 Sullivan PP, Moeng CH, Stevens B, Lenschow DH, Major SD (1998) Structure of the entrainment zone
650 capping the convective atmospheric boundary layer. J Atmos Sci 55:3042–3064
651 Tennekes H (1973) A model for the dynamics of the inversion above a convective boundary layer. J Atmos
652 Sci 30(4):558–566
653 Townsend AA (1980) The Structure of Turbulent Shear Flow. Cambridge University Press, 429 pp.
654 Turner J (1973) Buoyancy effects in fluids. Cambridge University Press, 367 pp.
655 Turner JS (1968) The influence of molecular diffusivity on turbulent entrainment across a density interface. J
656 Fluid Mech 33:639–656
657 Willis G, Deardorff JW (1974) A laboratory model of the unstable planetary boundary layer. J Atmos Sci
658 31:1297–1307
659 Wolanski EJ, Brush LM Jr (1975) Turbulent entrainment across stable density step structures. Tellus 27:259–
660 268
661 Wyngaard JC (2010) Turbulence in the Atmosphere. Cambridge University Press, 339 pp.
662 Wyngaard JC, Brost RA (1984) Top-down and bottom-up diffusion of a scalar in the convective boundary
663 layer. J Atmos Sci 41(14):102–112